applied sciences

MDPI

Article

Efficient Mercury Removal at Ultralow Metal Concentrations by Cysteine Functionalized Carbon-Coated Magnetite

Assadawoot Srikhaow [1], Teera Butburee [2], Weeraphat Pon-On [3], Toemsak Srikhirin [4], Kanchana Uraisin [5], Komkrit Suttiponpanit [6], Suwilai Chaveanghong [7] and Siwaporn Meejoo Smith [7,*]

[1] Materials Science and Engineering Graduate Program, Faculty of Science, Mahidol University, Rama VI Rd., Rajathevi, Bangkok 10400, Thailand; assadawoot.sri@gmail.com
[2] National Nanotechnology Center (NANOTEC), National Science and Technology Development Agency, 111 Thailand Science Park Phaholyothin Rd., Klong Nueng, Klong Luang, Pathumthani 12120, Thailand; teera.but@nanotec.or.th
[3] Department of Physics, Faculty of Science, Kasetsart University,50 Ngam Wong Wan Rd., Ladyaow, Chatuchak, Bangkok 10900, Thailand; fsciwpp@ku.ac.th
[4] Department of Physics, Faculty of Science, Mahidol University, Rama VI Rd., Rajathevi, Bangkok 10400, Thailand; toemsak.sri@mahidol.ac.th
[5] Department of Chemistry and Center of Excellence for Innovation in Chemistry, Faculty of Science, Mahidol University, Rama VI Rd., Rajathevi, Bangkok 10400, Thailand; kanchana.ura@mahidol.ac.th
[6] Environmental Technology Research Department, Innovation Institute, PTT Public Company Limited, 71/1 M.2 Phaholyothin Rd., Sanubtub, Wangnoi, Ayutthaya 13170, Thailand; komkrit.su@pttplc.com
[7] Center of Sustainable Energy and Green Materials and Department of Chemistry, 999 Phuttamonthon Sai 4 Rd, Salaya, Nakhon Pathom 73170, Thailand; suwilai.materialscience@gmail.com
* Correspondence: siwaporn.smi@mahidol.edu; Tel.: +66-2-4419817 (ext. 1171); Fax: +66-2354-7151

Received: 6 October 2020; Accepted: 19 November 2020; Published: 21 November 2020

Featured Application: This study highlights the utility of L-cysteine, a thiol-containing amino acid, as a functionalizing reagent for enhancing the adsorption capacity of Hg(II) ions by carbon-coated magnetite sorbents.

Abstract: This work reports the preparation and utility of cysteine-functionalized carbon-coated Fe_3O_4 materials (Cys-C@Fe_3O_4) as efficient sorbents for remediation of Hg(II)-contaminated water. Efficient removal (90%) of Hg(II) from 1000 ppb aqueous solutions is possible, at very low Cys-C@Fe_3O_4 sorbent loadings (0.01 g sorbent per liter of Hg(II) solution). At low metal concentrations (5–100 ppb Hg(II)), where adsorption is typically slow, Hg(II) removal efficiencies of 94–99.4% were achievable, resulting in final Hg(II) levels of <1.0 ppb. From adsorption isotherms, the Hg(II) adsorption capacity for Cys-C@Fe_3O_4 is 94.33 mg g^{-1}, around three times that of carbon-coated Fe_3O_4 material. The highest partition coefficient (PC) of 2312.5 $mgg^{-1}\mu M^{-1}$ was achieved at the initial Hg (II) concentration of 100 ppb, while significantly high PC values of 300 $mgg^{-1}\mu M^{-1}$ and above were also obtained in the ultralow concentration range (≤20 ppb). Cys-C@Fe_3O_4 exhibits excellent selectivity for Hg(II) when tested in the presence of Pb(II), Ni(II), and Cu(II) ions, is easily separable from aqueous media by application of an external magnet, and can be regenerated for three subsequent uses without compromising Hg(II) uptake. Derived from commercially available raw materials, it is highly possible to achieve large-scale production of the functional sorbent for practical applications.

Keywords: adsorption; magnetite; mercury; surface functionalization

1. Introduction

Mercury contamination of ground and surface water, and bioaccumulation of this heavy metal in aquatic and marine animals, presents serious concerns to public health and food safety worldwide [1–5]. Damage to the central nervous system, liver, kidneys, and heart in humans can be attributed to mercury exposure, the extent of which depends on the mercury form, dosage, and age and underlying health of the individual [6]. Major sources of environmental mercury contamination arise from waste effluents, such as those from mining, the chloralkali process, and petroleum industries [7]. Due to its acute toxicity, the World Health Organization (WHO) and European Union (EU) define permissible limits of total mercury in drinking water as being not greater than 1.0 ppb [8]. Based on literatures, though with its high toxicity, the number of papers reporting Hg(II) removal from water [9–23] have been found much less than those focused on other heavy metal pollutant such as ions of Cu, Pb, Zn, Cr, or Cd. Scopus-sorbents comparative details of the performance of several sorbents for Hg(II) removal are given, however, they are limited [12,13,24]. Besides, reports of effective sorbents for the removal of Hg(II) in water at low initial concentrations (≤100 ppb) are scarce [10,12–16]. Adsorption of Hg(II) has been found to be less effective at ultralow initial concentrations (≤20 ppb) [10] and is hampered due to the very small difference in Hg(II) concentration in solution relative to that at the sorption sites, resulting in very slow adsorption rates [25,26]. Therefore, treatment of Hg(II) contaminated water at such ultralow concentrations is very challenging, especially with the need to ensure quality levels comply with the WHO and EU permissible limits for drinking water (1.0 ppb) [8,26]. Commercially available and laboratory-scale synthetic activated carbon materials have been extensively reported as sorbents for Hg(II) ions, however, with low adsorption capacities (less than 20 mg/g) [24]. Recently, magnetic sorbents, i.e., zero-valent iron, magnetite (Fe_3O_4), and maghemite (γ-Fe_2O_3), easily recovered by application of an external magnetic field, have attracted great interest as effective sorbents for the removal of metal ions from water [17–22,27]. To enhance the stability of such sorbents, the magnetic core should be coated by a protective shell to avoid corrosion, as is possible at low pH or under other extreme conditions. Shell materials can be organic or inorganic, with stabilities dependent on the chemical nature of the material. For example, carbon shell coatings proved more stable than those of functionalized (chitosan, polyamidoamine, and mesoporous silica) materials at low/high pH and at high temperature/pressure [28–32]. Previously, Faulconer et al. [14] utilized a magnetic powdered activated carbon material at high sorbent dosage (1.0 g/L) in the adsorption of Hg(II) from aqueous solutions containing 100 ppb of the toxic metal. The Hg(II) removal efficiency was only 84% after 180 min, additionally having no evidence of the sorbent recyclability.

Effective sorbents for water remediation based on carbon-coated Fe_3O_4 materials have been fabricated recently, through one-step solvothermal treatment of an aqueous Fe(III) solution or aqueous Fe(III) and Fe(II) mixture in the presence of urea and glucose [29,33,34]. The high adsorption capacity of metal ions on these materials was due to the presence of oxygen-containing functional groups on the carbon surface, which electrostatically interact with metal ions. Surface oxygen functionalities can be further modified chemically, resulting in greater adsorption site density and, more importantly, the potential for selective metal ion adsorption. Enhanced adsorption capacities for metal ions have been demonstrated for sorbents functionalized with OH, C=O, COOH, NH, and SH groups, as in carboxyl-, ketoxime-, and 1-(2-thiazolylazo)-2-naphthol carbon-coated magnetite sorbents [35–37], as well as -$N(CH_2COOH)_2$-containing polymer/Fe_3O_4 composites [12] and mercapto-functionalized nano-Fe_3O_4 magnetic polymers [13].

This work describes the synthesis of a series of magnetic sorbents for removal of aqueous Hg(II) from water samples, over a wide concentration range (5–1000 ppb). Using a one-pot synthesis, carbon-coated Fe_3O_4 nanoparticles (C@Fe_3O_4) were obtained, and these were subjected to surface modification using L-cysteine, an amino acid with three functional groups (-SH_2, -NH_2, -COOH), to afford Cys-C@Fe_3O_4 particles. The Hg(II) removal efficiency of all sorbents (Fe_3O_4, C@Fe_3O_4, and Cys-C@Fe_3O_4) was examined under various conditions as part of a comprehensive study of the adsorption kinetics and thermodynamics, in addition to probing the selectivity of Hg(II) adsorption in the coexistence of other contaminant metal ions.

2. Materials and Methods

2.1. Chemicals

Iron (III) chloride hexahydrate ($FeCl_3 \bullet 6H_2O$, Sigma Aldrich), urea (Ajax Finechem), ethylene glycol (Ajax Finechem), D-glucose (Ajax Finechem), L-cysteine (Sigma Aldrich), mercury (II) nitrate monohydrate ($Hg(NO_3)_2 \bullet H_2O$, QRëC), thiourea (Ajax Finechem), sodium hydroxide (NaOH, Merck), and hydrochloric acid (HCl, 37% w/v, RCI Labscan) were of analytical grade and used as received. Ultrapure water, purified using a Millipore Milli-Q system (18 MΩcm), was used throughout the experiments.

2.2. Sample Preparation

Carbon-coated (Carbon@Fe_3O_4) nanoparticles were prepared using a solvothermal method reported by Zheng et al. [34]. Briefly, $FeCl_3 \bullet 6H_2O$ (0.8 g) was dissolved in 60 mL of ethylene glycol with stirring. After a clear solution was obtained, urea (3.0 g) and D-glucose (0.36 g) were added, and the mixture was stirred at room temperature for 30 min. Subsequently, the solution was transferred to a Teflon-lined stainless-steel autoclave and solvothermally treated at 200 °C for 12 h. Notably, previous works suggested that solvothermal temperatures of 160 °C and above are required to obtain a single phase of magnetite phase (Fe_3O_4) [29,38,39], and the boiling point of ethylene glycol is elevated due to the elevated pressure in the reactor and the colligative property of solutions [40–42]. After cooling down to room temperature and washing sequentially with ultrapure water and ethanol (each three times), the resulting carbon-coated Fe_3O_4 nanoparticles were magnetically separated from the solution using a neodymium magnet and dried at 60 °C in a vacuum oven (SHEL LAB, Shelton Manufacturing, Inc., Cornelius, Oregon) for 12 h. Uncoated Fe_3O_4 nanoparticles were synthesized from a solvothermal treatment of a $FeCl_3$/EG/urea mixture (without addition of D-glucose). Cysteine-functionalized (Cys-C@Fe_3O_4) particles were synthesized using a modified version of the protocol previously utilized in functionalization of iron oxide materials [43,44]. In a typical synthesis, an aqueous suspension of C@Fe_3O_4 nanoparticles (1.0 g in 100 mL) was ultrasonically treated for 30 min, and then mixed with an aqueous solution of L-cysteine (250–1000 mg dissolved in 100 mL). The pH of the suspension was adjusted to 5.8 using 0.1 M HCl or 0.1 M NaOH, followed by stirring for 12 h under an N_2 atmosphere at room temperature. The solid products were then separated using an external magnet, and cleaned by washing sequentially with water and ethanol (each three times). The particles were then vacuum dried at 60 °C for 12 h and were denoted as either 250Cys-C@Fe_3O_4, 500Cys-C@Fe_3O_4, or 1000Cys-C@Fe_3O_4, with the number reflecting the weight of L-cysteine added in the preparation. Scheme S1 (Supporting Information) summarizes sample preparation methods used in this study.

2.3. Sample Characterization

Powder X-ray diffraction (PXRD) measurements were conducted on a Bruker powder X-ray diffractometer (AXS model D8 advance) with Cu Kα radiation, $\lambda = 1.5418$ Å, 3-s step time and 0.075° step size. Fourier-transform infrared spectroscopy (FTIR) was measured over a range of 480–4000 cm^{-1} using a Perkin Elmer Fourier-transform infrared spectrometer (Spectrum GX FT-IR System). Thermogravimetric analyses (TGA) were performed on a TA Instruments thermogravimetric analyzer (SDT 2960 Simultaneous DSC-TGA), with samples heated from 25 to 800 °C (heating rate 20 °C/min) under an N_2 atmosphere. Magnetic properties of samples were investigated using a Lakeshore vibrating sample magnetometer (VSM 7404) at room temperature (applied field −6000 to 6000 Oersted). Transmission electron microscopy (TEM) and high-resolution TEM were carried out on a JEOL transmission electron microscope (2100), operated at 200 keV. Zeta potential measurements were performed on a Malvern Instruments zeta potential analyzer (Zetasizer, Nano ZS), in water at

25 °C. Surface properties of sorbents were examined using N_2 sorption on a Quantachrome Instrument (Nova 2000e). All samples were degassed at 200 °C for 10 h prior to measurements. Quantification of cysteine loading in Cys-C@Fe_3O_4 particles was obtained through combustion sulfur analysis using a LECO (CHNS-628S) elemental analyzer.

2.4. Hg(II) Adsorption Test

The Hg(II) adsorption capacity of sorbents was examined using the following procedure. Typically, 1 mg of the sorbent was dispersed into 100 mL of aqueous 1000 ppb Hg(II) (synthetic wastewater) in a polypropylene bottle. The suspension was shaken with a thermostatic shaker at 25 °C and aliquots were removed at regular time intervals, with dispersed sorbent removed from the aliquot using a magnet. The liquid sample was then stabilized by addition of 5% (w/v) $KMnO_4$ solution, then mixing with 1% (v/v) HCl solution. Prior to determination of the Hg(II) content, addition of sufficient amount of 12% (w/v) hydroxylamine aqueous solution is required to remove the excess $KMnO_4$ and to acquire clear solutions. Atomic absorption spectroscopy (Perkin Elmer, AAnalyst 200 equipped with FIAS 100 system) was utilized to determine the concentration of Hg(II) in the aliquot sample, through coupling with flow injection analysis system-hydride generation (FIAS-HG) (reductant 0.2% (w/v) NaBH4 in 0.05% (w/v) NaOH, carrier solution 3% (v/v) HCl). The Hg(II) removal efficiency (%) [10,12] or breakthrough (BT, %) [45] was calculated according to the formula

$$\text{Removal efficiency (\%)} = (C_0 - C_t/C_0) \times 100\%, \tag{1}$$

where C_0 (mg L^{-1}) is the initial concentration of Hg(II) and C_t (mg L^{-1}) is the concentration of Hg(II) ions after adsorption

The mercury uptake (q_e, mg g^{-1}), and removal efficiency, was calculated according to the equation:

$$q_e = ((C_0 - C_e) \times V)/m, \tag{2}$$

where C_0 is the initial mercury concentration in solution (mg L^{-1}), C_e is the equilibrium concentration of mercury (mg L^{-1}) after adsorption, V is the volume of the solution (0.1 L; in this study), and m is the weight of the sorbent used (g). The 500Cys-C@Fe_3O_4 sample was employed to study pH dependence of Hg(II) removal, while HCl and NaOH were added for pH adjustment.

In addition, partition coefficients (PC, mg g^{-1} μM^{-1}) were evaluated using the adsorption capacity or the mercury uptake (q_e, mg g^{-1}) divided by the equilibrium concentration of mercury (μM) after adsorption [4,46].

$$PC = (q_e/C_e). \tag{3}$$

3. Results and Discussion

3.1. Sample Characterization

TEM images of uncoated Fe_3O_4 and C@Fe_3O_4 (Figure 1a,b) show individual particles to be spherical, although these undergo aggregation. Uncoated Fe_3O_4 particles are larger (diameter 40–70 nm) than those of C@Fe_3O_4. This finding is consistent with previous work reported by Zheng et al. [34] and Pham et al. [47]. With the addition of D-glucose in the reaction media, a thin carbon shell coating clusters of the magnetite particles are formed (cluster size 50–80 nm, Figure 1b). HRTEM (Figure 1c) reveals nanostructural detail of these C@Fe_3O_4 clusters, highlighting the amorphous carbon layer and crystalline nature of the magnetite core, as indicated by the lattice spacing (0.29 nm) being consistent with the (002) plane of magnetite [48]. The smaller size of C@Fe_3O_4 particles relative to uncoated Fe_3O_4 suggests that glucose acts as both a precursor of carbon shell formation and crystallization inhibitor, resulting in slow Fe_3O_4 crystal growth. L-Cysteine loading appears to have no effect on the Cys-C@Fe_3O_4 cluster size and the size of Fe_3O_4 particles (Figure 2), reflecting the stability of carbon-coated magnetite towards surface functionalization.

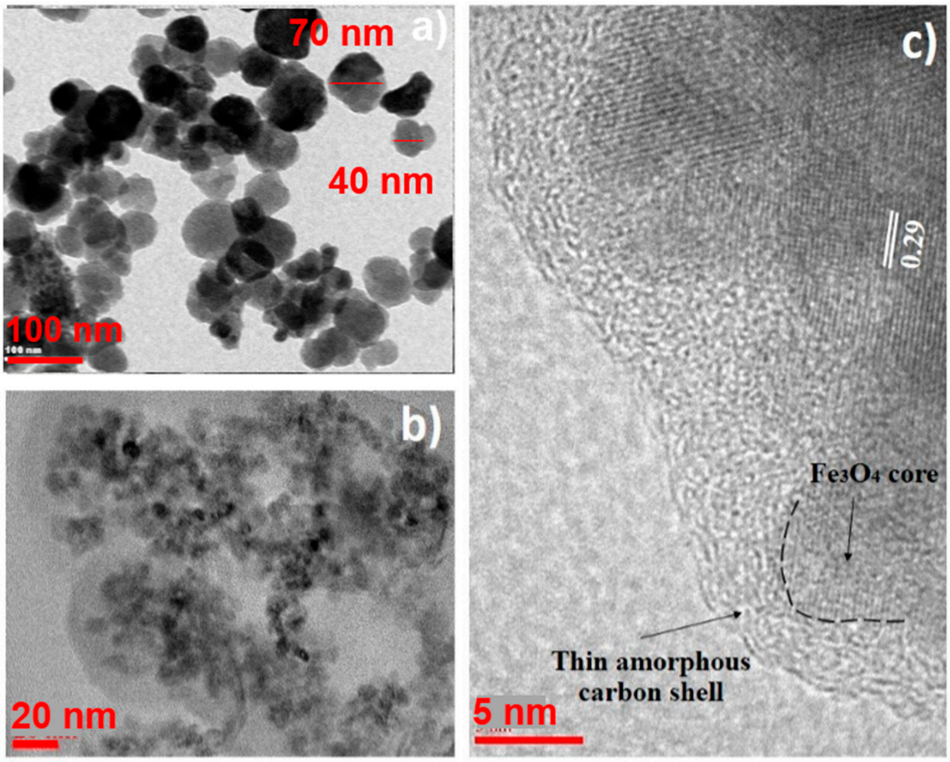

Figure 1. TEM images of (**a**) uncoated Fe_3O_4, (**b**) C@Fe_3O_4, and (**c**) C@Fe_3O_4.

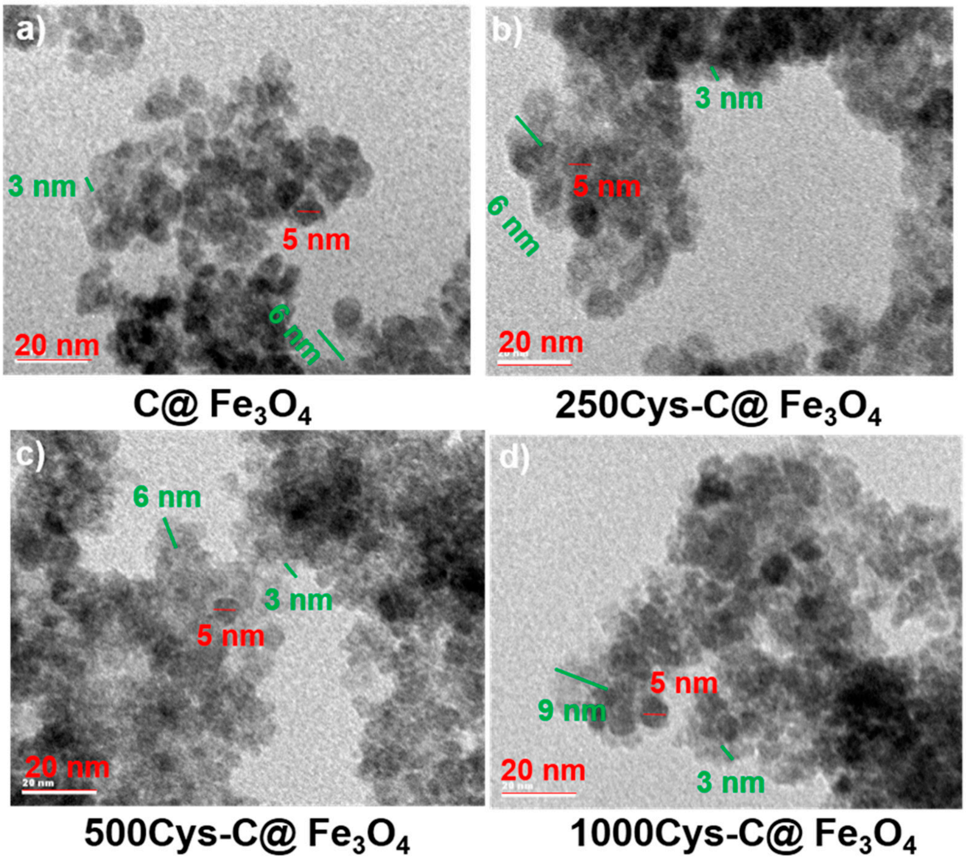

C@ Fe_3O_4

250Cys-C@ Fe_3O_4

500Cys-C@ Fe_3O_4

1000Cys-C@ Fe_3O_4

Figure 2. TEM images of (**a**) C@Fe_3O_4, (**b**) 250Cys-C@Fe_3O_4, (**c**) 500Cys-C@Fe_3O_4, and (**d**) 1000Cys-C@Fe_3O_4.

Figure 3a shows PXRD patterns of uncoated Fe_3O_4, C@Fe_3O_4, and Cys-C@Fe3O4 particles and that of bulk L-cysteine for comparison. The characteristic peaks of magnetite (Fe_3O_4, cubic phase, JCPDS file No. 75-1609) [36,48] appear in the diffraction patterns of all particles. However, the intensity of these magnetite peaks in C@Fe_3O_4 and Cys-C@Fe_3O_4 samples is significantly lower than those in uncoated Fe_3O_4, possibly related to shielding by the surface layers [49]. XRD peaks corresponding to graphitic carbon were not observed in C@Fe_3O_4 and Cys-C@Fe_3O_4, suggestive of amorphous carbon coatings in agreement with HRTEM observations. Additional XRD peaks corresponding to crystalline cysteine (2-theta: 18.3°, 28.5°, 31.4°, and 34.2°) being observed in 1000Cys-C@Fe_3O_4 is probably the result from excess cysteine deposited on the carbon shell.

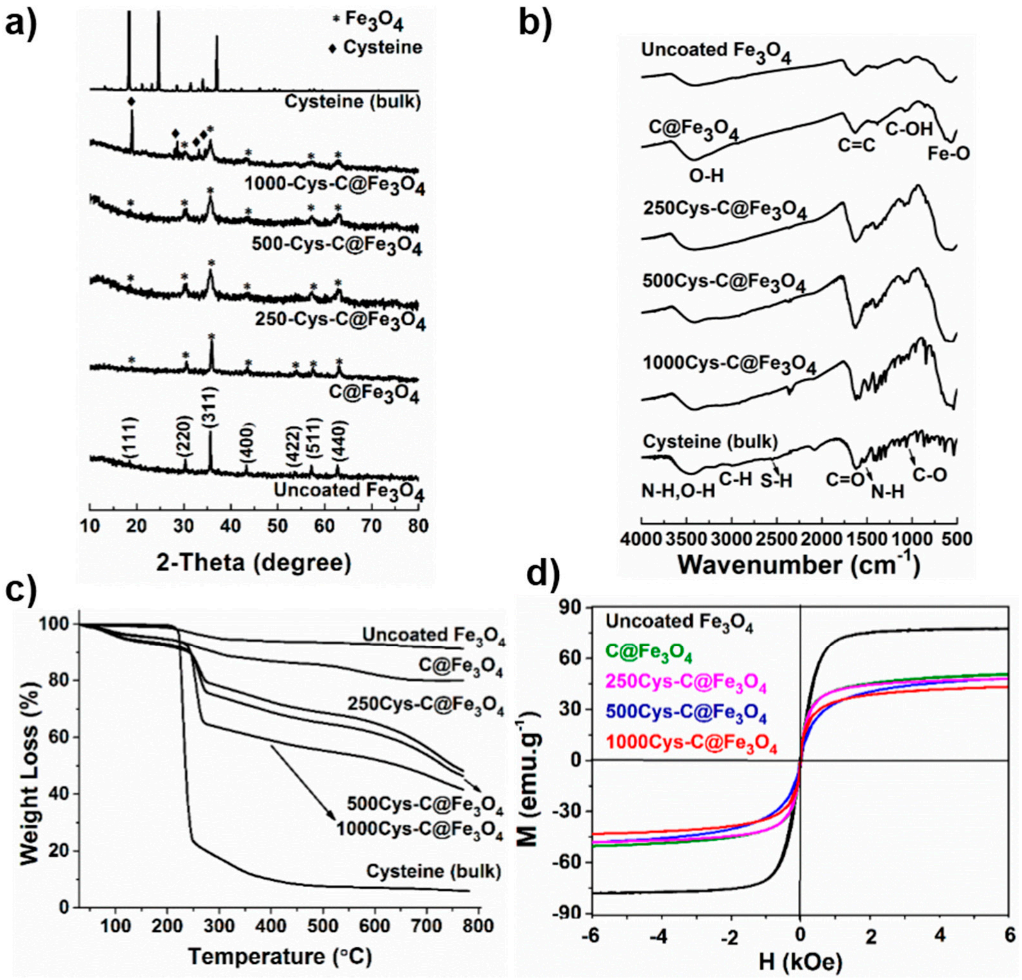

Figure 3. (**a**) Powder X-ray diffraction (PXRD) patterns, (**b**) FTIR spectra, (**c**) thermogravimetric (TG) curves, and (**d**) magnetic behavior of uncoated Fe_3O_4, C@ Fe_3O_4, and Cys-C@Fe_3O_4 materials. The Y axis in (**a**,**b**) are given in arbitrary unit.

The surface functionality of prepared sorbents was probed using FTIR. As shown in Figure 3b, the characteristic Fe-O stretching vibration appears at 570 cm^{-1} in all Fe_3O_4-based samples [36]. Peaks corresponding to C-OH stretching and O-H bending (1069 cm^{-1}) occur in C@Fe_3O_4, with C=C vibrations at 1620 cm^{-1} reflecting the successful carbonization of glucose to the coating layer [29]. Moreover, the relative intensity of the O-H vibration (3600–3100 cm^{-1}) is significantly higher in C@Fe_3O_4 samples relative to uncoated magnetite, indicating the greater abundance of these groups on the carbonized surface. The existence of these surface groups facilitates appendage of metal binding functionalities, in this case L-cysteine, to the particle periphery [34]. For Cys-C@Fe_3O_4 samples, the presence of L-cysteine was confirmed by the N-H vibration overlapping with the O-H stretching frequency at 3600–3100 cm^{-1}, and two bands at 1600 cm^{-1} and 1240 cm^{-1} attributed to C=O and C-O stretching of the amino acid, respectively [29]. Moreover, further peaks at ~1500 cm^{-1} (N-H bending) and 2590 cm^{-1} (S-H stretching) are evident. These results confirm the grafting of L-cysteine to the particle surface, which most likely occurs via condensation between surface hydroxyl groups and the carboxylic acid moiety in L-cysteine [50]. CHNS analysis results were employed to confirm the presence of cysteine and to determine the cysteine content in Cys-C@Fe_3O_4 samples. These results suggest that cysteine content increases with cysteine loading, as found to be 0.0563, 0.0963, and 0.1828 mmol per gram of solid samples of the 250Cys-C@Fe_3O_4, 500Cys-C@Fe_3O_4, and 1000Cys-C@Fe_3O_4, respectively.

Thermogravimetric (TG) analysis plots for all particle systems and that of bulk cysteine are illustrated in Figure 3c. The TGA profile of uncoated Fe_3O_4 shows around 2% weight loss between 100 and 400 °C, possibly due to loss of residual water and surface hydroxyl groups. On the other hand, three distinct weight loss steps are evident for C@Fe_3O_4: 40–200, 200, and >500 °C, corresponding to the loss of surface hydroxyl groups and water molecules and the combustion of amorphous carbon shells [34]. In addition, the TGA curve of bulk cysteine highlights decomposition occurring between 200 and 450 °C, while those of Cys-C@Fe_3O_4 particles show three weight loss steps, below 230, 230–270, and >500 °C, which coincide with the loss of residual water and hydroxyl groups, cysteine decomposition, and the decomposition of the carbon shell, respectively [33,50]. With no change in weight after 680 °C, the total weight loss results are indicative of 81% wt./wt. Fe_3O_4 in C@Fe_3O_4 material. On the other hand, the steep slopes at around 800 °C in in TG plots of 250Cys-C@Fe_3O_4, 500Cys-C@Fe_3O_4, and 1000Cys-C@Fe_3O_4 systems indicate slower combustion (compared with C@Fe_3O_4), suggesting superior thermal stability arising from the presence of the cysteine layer. Furthermore, the residual mass of solid samples at 800 °C suggests the content of Fe_3O_4 in 250Cys-C@Fe_3O_4, 500Cys-C@Fe_3O_4, and 1000Cys-C@Fe_3O_4 to be not more than 50%, 49%, and 40% wt./wt., respectively, and reflect the increase in cysteine content with initial loading level, as indicated from elemental sulfur analysis. Magnetic properties of all Fe_3O_4-based samples were examined using VSM at room temperature. Results depicted in Figure 3d show that the saturation magnetization of uncoated Fe_3O_4, C@Fe_3O_4, 250Cys-C@Fe_3O_4, 500Cys-C@Fe_3O_4, and 1000Cys-C@Fe_3O_4 samples were about 78, 51, 50, 49, and 45 emu.g^{-1}, respectively. Reductions in saturation magnetization after carbon coating and cysteine functionalization can be attributed to the decreasing fraction of magnetic material in these particles relative to diamagnetic coating materials (carbon and cysteine) [50,51].

Figure S1 shows N_2 adsorption–desorption isotherms and pore size distributions of all samples, with porous structural data listed in Table 1. It can be concluded that isotherms of all materials are of type-IV with a type-H3 hysteresis loop, typical of mesoporous materials [51]. The greater specific area of C@Fe_3O_4 (90 m^2.g^{-1}) over that of uncoated Fe_3O_4 (55 m^2.g^{-1}) may be a consequence of the presence of pores in the carbon coating. Cysteine-modified C@Fe_3O_4 samples show lower specific surface areas and total pore volumes than C@Fe_3O_4 due to grafting of the surface L-cysteine ligands, which results in blockage of surface channels and reduced porosity [52,53].

Table 1. Porous structural data for as-synthesized samples (S_{BET}, specific surface area by BET; V_t, total pore volume; D_a, average pore diameter).

Sample	S_{BET} (m^2·g^{-1})	V_t (cm^3·g^{-1})	D_a (nm)
Uncoated Fe_3O_4	55	0.07	2.28
C@Fe_3O_4	90	0.11	2.24
250Cys-C@Fe_3O_4	30	0.04	2.44
500Cys-C@Fe_3O_4	23	0.03	2.52
1000Cys-C@Fe_3O_4	40	0.04	2.56

3.2. Adsorption Kinetics

Figure 4 reports that at the initial Hg(II) concentration of 1000 ppb, 100% breakthrough (BT) was not achievable for all of the studied sorbents after 60 min treatments. Low %BT values (<30%) for C@ Fe_3O_4 and uncoated Fe_3O_4 were obtained even after 60 min treatments. On the other hand, 90% BT (q_e = 90.03 mg g^{-1}) for 500 Cys-C@ Fe_3O_4 were obtained after treatments for 45 min and above, while about 40%BT (q_e = 42.0 mg g^{-1}) was achieved after 5 min. At BT time of 60 min, the %BT follows the order of 500Cys-C@Fe_3O_4 > 1000 Cys-C@Fe_3O_4 > 250 Cys-C@ Fe_3O_4 >> C@ Fe_3O_4 > uncoated Fe_3O_4, being consistent with the specific surface area, surface functional groups, and adsorption capacity relationship previously discussed. Notably, times to reach 10%BT, 50%BT, and 90%BT of the prepared magnetic sorbents, interpolated from Figure 4, are reported in Table S1. After 60 min of 500 Cys-C@ Fe_3O_4 treatments, 50%BT and 90%BT were achievable, respectively, at pH = 2 and pH ≥ 6 (Figure S2 and Table S2).

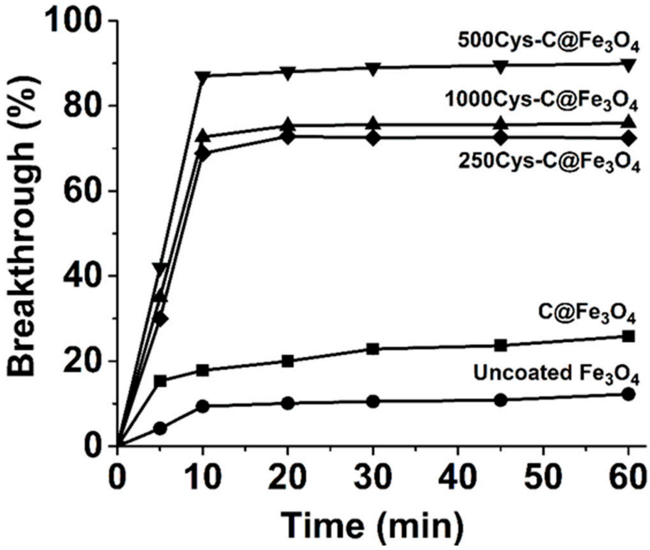

Figure 4. Hg(II) treatment time dependence of % Breakthrough (BT) at initial Hg(II) concentration of 1000 ppb and sorbent loading of 0.01 g L^{-1}. High reproducibility of the measurements is indicated by small standard deviations from five identical batch experiments.

Kinetic results for Hg(II) adsorption, measured using 0.01 mg L^{-1} sorbent suspended in 1000 ppb Hg(II) aqueous solution at pH 6, are illustrated in Figure 5a. For all samples, high Hg adsorption rate was observed during the first 10 min and reached an equilibrium after 20 min. The greater adsorption efficiency of C@Fe_3O_4 relative to uncoated magnetite is likely due to the presence of surface hydroxyl groups, and its higher surface area. For Cys-C@Fe_3O_4 samples, which exhibit lower surface area than C@Fe_3O_4, the relatively high adsorption capacity is related to the metal-chelating ability of the -NH_2 and -SH functional groups in the appended L-cysteine. Notably, the highest Hg uptake was 90 mg.g^{-1} by 500Cys-C@Fe_3O_4. Further increases in cysteine content (1000Cys-C@Fe_3O_4) resulted in lower Hg(II) removal efficiency, likely due to the deposition of bulk cysteine on the carbon shell (XRD result, Figure 3a) that could inhibit effective adsorption by internal pores. Mercury removal experiments were further conducted for longer periods (60 min) to ensure adsorption saturation. To study the adsorption mechanism, 500Cys-C@Fe_3O_4, which exhibits the highest level of Hg(II) uptake, was selected as representative of Cys-C@Fe_3O_4, along with uncoated Fe_3O_4 and C@Fe_3O_4 for comparison. Pseudo-second-order kinetic models (Figure 5b) were then applied to probe the mechanism [33,54]. The correlation coefficients for the pseudo-second-order kinetic model are very close to 1, and the calculated equilibrium adsorption capacities ($q_{e,cal}$) derived from this model are also much closer to the experimentally determined adsorption capacities ($q_{e,exp}$) than that derived using the pseudo first order kinetic model. These results also support the assumption that sorption should occur through chemical adsorption rather than mass transport [55].

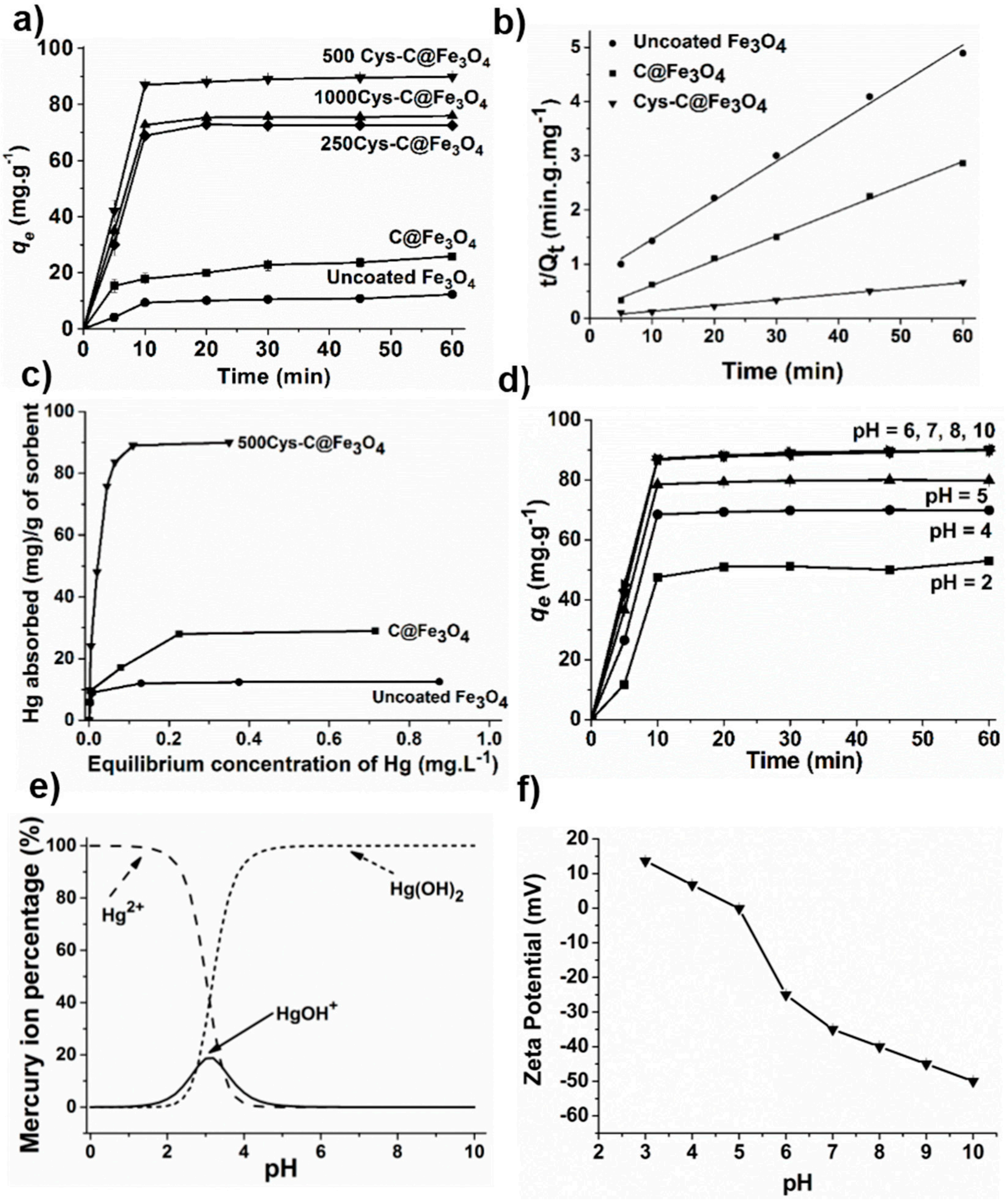

Figure 5. (**a**) Adsorption kinetics; (**b**) pseudo-second-order kinetic plot for Hg(II) adsorption; (**c**) Langmuir adsorption isotherms of uncoated Fe_3O_4, C@Fe_3O_4, and Cys-C@Fe_3O_4; (**d**) effect of pH on Hg(II) adsorption by 500Cys-C@Fe_3O_4; (**e**) Hg ion speciation diagram with pH as simulated using the Visual MINTEQ 3.1 software (C_{Hg}(total) = 1000 ppb); and (**f**) zeta potential of 500Cys-C@ Fe_3O_4 particles at different pH values. Small standard deviations from five identical batch experiments shown in Figure 5a,d implied the high data reproducibility.

3.3. Adsorption Isotherm

The relationship between the equilibrated mercury uptake (q_e) of sorbent particles and the equilibrated concentration of Hg(II) in solution (C_e) was used to quantitatively describe the sorption, by way of adsorption isotherms. In this case, experiments were performed under conditions as used in the kinetic studies, but initial Hg(II) concentrations were varied from 60 to 1000 ppb. The adsorption time of 60 min is sufficient for adsorption–desorption equilibrium, as the difference in Hg(II) uptake from 60 min treatments and from longer treatment time was found negligible. As depicted in Figure 5c, Hg(II) uptake increased with initial Hg(II) concentration until it reached a saturation point. According to these profiles, the saturated adsorption capacities of uncoated Fe_3O_4, C@Fe_3O_4, and 500Cys-C@Fe_3O_4 were 12, 28, and 90 mg g^{-1}, respectively. The equilibrium data were then fitted using the Langmuir model (Figure S3a), allowing prediction of equilibrium parameters [56].

$$S_{ad} = N_{\max} \times (S_{aq}/(K^{-1} + S_{aq})). \tag{4}$$

In Equation (4), S_{ad} is the number of ions adsorbed per unit area of sorbent surface (mg g^{-1}), S_{aq} is the equilibrium concentration of ions in solution (mg L^{-1}), $N_{\max}$ is the maximum adsorption capacity (mg g^{-1}) corresponding to complete monolayer coverage on the sorbent surface, and K is the Langmuir adsorption constant (L mol^{-1}) related to binding strength. From fitting results shown in Table 2 and comparisons with results calculated using the Freundlich model [15] (data shown in Figure S3b), adsorption clearly follows Langmuir behavior indicating formation of a uniform monolayer of metal ions adsorbed on the particle surface [50]. Furthermore, it is important to note that the calculated maximum adsorption capacity of uncoated Fe_3O_4 (12.56 mg g^{-1}) is enhanced by carbon coating (29.85 mg g^{-1}) and more so, by cysteine functionalization (94.33 mg g^{-1}).

Table 2. Adsorption isotherm parameters and sorption rate constants for Hg(II) adsorbed on uncoated Fe_3O_4, C@ Fe_3O_4, and 500Cys-C@ Fe_3O_4.

	Uncoated Fe_3O_4	**C@ Fe_3O_4**	**500Cys-C@ Fe_3O_4**
Langmuir model			
$q_{e(exp)}$ (mg.g^{-1})	12.27	21.01	90.03
Pseudo-first-order model			
K_1 (min^{-1})	0.028	0.034	0.041
$q_{e(cal)}$ (mg.g^{-1})	9.526	7.874	35.07
R^2	0.986	0.945	0.601
Pseudo-second-order model			
K_2 (g.mg^{-1}.min^{-1})	0.007	0.014	0.004
$q_{e(cal)}$ (mg.g^{-1})	13.95	22.03	95.24
R^2	0.998	0.998	0.995
Freundlich model			
K_f (mg.g^{-1})	11.12	35.11	265.58
n	7.41	3.86	1.98
R^2	0.8212	0.9626	0.9100

3.4. Effect of pH on Hg(II) Adsorption

Figure 5a,d both showed that the Hg uptake reached maximum Hg(II) uptake values after 20 min. Figure 5d shows the effect of pH on Hg(II) adsorption by 500Cys-C@Fe_3O_4, revealing that removal capacity is highly pH dependent. The aqueous formation of charged Hg(II) species (Hg^{2+}, $HgOH^+$) and neutral $Hg(OH)_2$ can result at different pH values, although these are all capable of reacting with L-cysteine thiol groups due to the high affinity of Hg for sulfur [31]. As shown in Figure 5e, speciation curves calculated using the Visual MINTEQ software [26] indicate that free Hg(II) ions predominate at pH ≤ 2, which in the presence of thiol groups may form positively charged complexes (S-Hg^+). The presence of large numbers of such complexes on the sorbent surface may, at some point, inhibit further binding based on electrostatic repulsion. At higher pH values mercuric hydroxide species ($HgOH^+$ and $Hg(OH)_2$)) become more prevalent, which are able to bind to cysteine thiol groups forming neutral complexes (−S−HgOH) [57]. The buildup of uncharged Hg(II) complexes on the sorbent surface does not retard further Hg(II) adsorption in the same way as accumulation of positive charge. Accordingly, 500Cys-C@Fe_3O_4 exhibits greater Hg(II) removal performance at higher pH values, as shown in Figure 5d. These findings are in agreement with zeta potential measurements with 500Cys-C@Fe_3O_4 (Figure 5f), which indicate that the particle surface is positively charged at a solution pH lower than the Point Zero Charge (*PZC*, ~5.4) and becomes negatively charged only above this value.

3.5. Adsorption of Hg(II) at Ultralow Concentrations

To further demonstrate the efficiency of 500Cys-C@Fe_3O_4 for Hg(II) removal, adsorption studies were conducted using ultralow Hg(II) concentrations. Adsorption experiments using Hg(II) concentrations ranging from 100 to 5 ppb (pH 6) demonstrated the performance of 500Cys-C@Fe_3O_4, with >99% Hg(II) removal being possible in 1 h over the entire concentration range, from 100, 50, 20, 10, and 5 ppb to 0.86, 0.45, 0.36, 0.34, and 0.31 ppb, respectively. These final Hg(II) concentrations were less than 1 ppb, meeting acceptable limits for drinking water set down by the WHO and EU [8].

3.6. Selectivity of 500Cys-C@Fe_3O_4 Sorbent

Many types of metal ions coexist in real water samples; competitive binding of these with Hg(II) to sorbents is, therefore, a serious issue potentially governing sorbent performance. In this work, three contaminant metal ions commonly found in industrial wastewater [58,59], Cu(II), Pb(II), and Ni(II), were selected as the basis for competitive adsorption studies against Hg(II) using 500Cys-C@Fe_3O_4. As seen in Table 3, these ions have negligible effect towards the adsorption of Hg(II). This can be rationalized using the Hard–Soft Acid–Base (HSAB) theory: Hg(II) is considered as a soft metal (relatively large ionic size, low electronegativity, and high polarizability) with higher affinity for soft donor atoms (such as sulfur) than relatively hard metal ions (Cu(II), Pb(II), and Ni(II)) [60].

Table 3. Concentrations of Hg(II) Pb(II), Ni(II), and Cu(II) ions in a simulated wastewater before and after treatment with 500Cys-C@Fe_3O_4 sorbent. The concentrations of each metal ion in the treated wastewater shows the amount of residual metal contaminants after adsorption.

	Metal Ion Concentration (ppb)			
	Hg(II)	**Pb(II)**	**Ni(II)**	**Cu(II)**
Before adsorption	1000.0	500.8	505.3	501.3
After adsorption	105.4	495.6	497.7	494.4
Removal efficiency	89.5%	1.0%	1.5%	1.3%

3.7. Determination of Thermodynamic Parameters

To study the thermodynamics of Hg(II) adsorption, a series of adsorption tests were performed, each using 1.0 mg of 500Cys-C@Fe_3O_4 with 100 mL of 1000 ppb Hg(II) solution at different temperatures (25, 35, or 40 °C). The thermodynamic feasibility and spontaneous nature of the adsorption process were assessed based on thermodynamic parameters including the standard Gibbs free energy (ΔG°), enthalpy change (ΔH°), and entropy change (ΔS°), as determined from the following equations [54,55,57].

$$\Delta G^\circ = -RT \ln K_d \tag{5}$$

$$\ln K_d = (\Delta S^\circ/R) - (\Delta H^\circ/RT) \tag{6}$$

$$K_d = q_e/C_e, \tag{7}$$

where K_d is the distribution coefficient of adsorption, R is the universal gas constant (8.314 $J.mol^{-1}.K^{-1}$), and T is the absolute temperature (K). q_e and C_e are the mercury uptake and equilibrium concentration of mercury ($mg.L^{-1}$) after adsorption, respectively (see Experimental section). Values of ΔH° (−24.1 kJ mol^{-1}) and ΔS° (−72.7 J mol^{-1} K^{-1}) were quantified from the slope and intercept of the linear van't Hoff plot, as seen in Figure S4. The values of ΔG° (−2.93 kJ mol^{-1} at 298 K, −1.70 kJ mol^{-1} at 308 K, and −1.27 kJ mol^{-1} at 313 K) suggest that Hg(II) adsorption on the cysteine functionalized carbon-coated magnetite is thermodynamically feasible. The decrease in −ΔG° with increasing temperature reveals that the sorption process is exothermic and more favorable at lower temperatures, similar to previous work [15,55]. Joen et al. [61] has suggested that escape of mercury ions from surface sites is more facile at higher temperature. The negative value of ΔH° indicates that Hg(II) sorption is exothermic at 25–40 °C. The value of ΔS° is also negative, suggesting a decrease in randomness at the solid/solution interface during Hg(II) sorption.

3.8. Sorbent Recyclability

As shown in the Figure 6 inset, 500Cys-C@Fe_3O_4 sorbent can be well dispersed in aqueous media and can be harvested easily by magnetic separation. Desorption of Hg(II) from the sorbent surface was examined to provide a measure of sorbent stability and recyclability, both being important parameters for industrial applications. For 500Cys-C@Fe_3O_4, experiments were conducted using an eluent solution (10 mL) composed of 0.1 M HCl and 5% (w/v) thiourea. Prior to measurements, the used sorbent was washed three times with deionized water. After adding the eluent solution to the used sorbent, desorption was allowed to proceed by shaking the suspension for 1 h at a constant temperature. It is possible that dissolution of magnetite particles could occur during desorption under the experimental conditions. Atomic absorption spectroscopy of the eluent solution after the first desorption cycle indicated an Fe concentration of 0.34 ppm for 500Cys-C@Fe_3O_4, and 0.51 ppm and 5.94 ppm for C@Fe_3O_4 and uncoated Fe_3O_4 nanoparticles, respectively, highlighting the importance of the surface coating on maintaining core integrity. Results of desorption and adsorption for five cycles using the 500Cys-C@Fe_3O_4 sorbent are shown in Figure 6. These reveal that the sorbent maintains high desorption efficiency (90%) and Hg uptake (90 mg.g^{-1}) performance over the first three cycles. However, adsorption efficiencies significantly decreased for the fourth and fifth cycles, while the desorption efficiency only slightly decreased. This behavior could result from saturation of the binding sites and/or degradation of bound cysteine moieties at low pH [62,63].

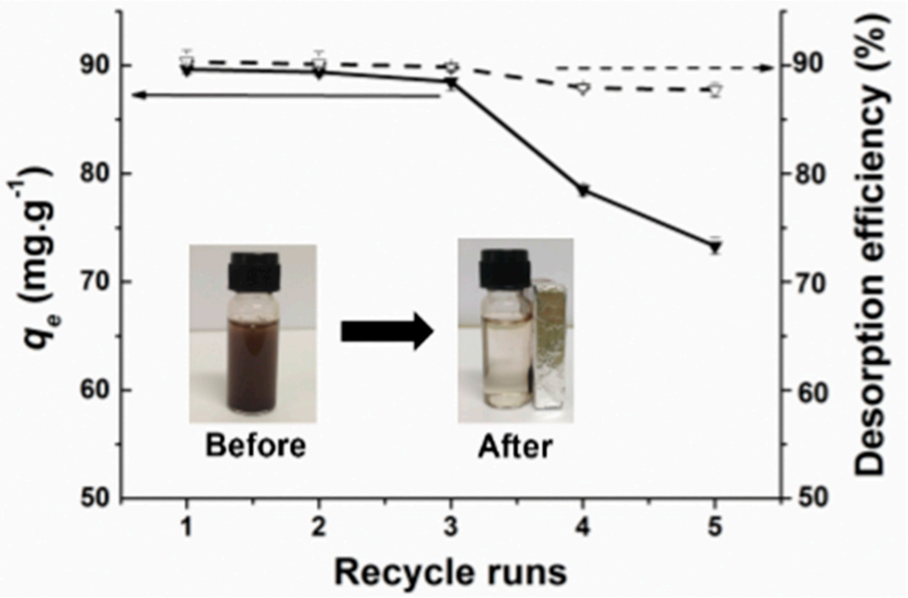

Figure 6. Hg(II) uptake (solid line) and percentage Hg(II) desorbed (dashed line) over five adsorption/desorption cycles using 500Cys-C@Fe_3O_4 sorbent. The inset shows the separation of the material from the aqueous media using an external magnetic field.

Table 4 highlights examples of sorbents applied to removal of ultralow concentrations (<20 ppb of Hg(II)), in comparison to 500Cys-C@Fe_3O_4 material. From these, 500Cys-C@Fe_3O_4 shows comparable performance at much lower sorbent loadings, although longer contact times were employed in this work. Thio-silica-coated magnetite required very low sorbent loadings for Hg(II) removal, but its preparation is more complex, requiring more steps than that needed for Cys-C@Fe_3O_4 [15]. Acrylamide-hydroxyl-MOFs [10] and MOF-74-Zn [16] show lower removal efficiencies using higher sorbent loadings and are nonmagnetic, thus cannot be separated for reuse by an application of an external magnet. Furthermore, the adsorption capacity and satisfactory level of sorbent performance in removal of ultralow concentrations of Hg(II) based on the WHO and EU drinking water standards is reported in Table 5, in which 500Cys-C@Fe_3O_4 material shows superior comparative performance at low sorbent loadings.

Table 4. Comparison of adsorption capacities of sorbents towards Hg(II) removal from dilute aqueous metal solutions (100 ppb ≥ (Hg(II)).

Sorbent	Concentration (ppb)	Loading ($g.L^{-1}$)	Contact Time (min)	Removal Efficiency
Cys-C@Fe_3O_4 (this work)	5–100 1000	0.01 0.01	60 10	94–99.4% 90%
2-mercapto-benzothiazole Fe_3O_4 composite [13]	5–200	1.00	4	92–99%
$N(CH_2COOH)_2$ containing polymer/Fe_3O_4 composite [12]	5–50	0.40	10	~98%
Magnetic powdered activated carbon [14]	100	1.00	180	84%
Thiol-silica-coated magnetite [15]	80	0.008	15	100%
Acrylamide-hydroxyl-MOFs [10]	100	0.05	60	80%
MOF-74-Zn [16]	20–50	0.10	120	54–72.3%

Comparative PC values of 500 Cys-C@Fe_3O_4 material, at varying initial Hg(II) concentrations (5–1000 ppb), were evaluated using Equation (2). They are reported in Table 5. The obtained PC values of the developed magnetic material at the studied Hg(II) concentration range were found being much higher than other sorbents. In particular, the significantly high PC values of the Cys-C@Fe_3O_4 material at ultralow Hg(II) initial concentrations (≤20 ppb) should be attributed to the high chelating ability of Hg(II) ions and the -NH_2 and -SH functional groups present on the surface of magnetic material.

Table 5. Comparative sorption capacities, Hg concentrations before and after treatment, Hg uptake, and partition coefficient values for various sorbents for Hg(II) removal at ultralow metal concentrations. The numbers in bold indicate the Hg(II) concentration lower than the World Health Organization (WHO) and European Union (EU) permissible limits of total mercury in drinking water. Note that n.d. is denoted as not determined as the volume of treated Hg(II) solution is unknown, while n.a is denoted as not applied due to the partition coefficient (PC) value is infinity using Equation (3).

Sorbent	**N_{max} (mg.g^{-1})**	**Sorbent Loading (g.L^{-1})**	**Initial Hg Concentration (ppb)**	**Final Hg Concentration (ppb)**	**q_e (mgg^{-1})**	**PC (mgg^{-1}μM^{-1})**
500Cys-C@Fe_3O_4 (this work)	94.33	0.01	1000	105	89.5	171.0
			100	**0.86**	9.9	2312.4
			50	**0.45**	5.0	2208.7
			20	**0.36**	2.0	1094.3
			10	**0.34**	1.0	569.9
			5	**0.31**	0.5	303.5
2-mercapto- benzothiazole Fe_3O_4 composite [13]	0.59	2.00	100	2.20	0.050	4.45
			50	**0.70**	0.025	7.1
			20	**0.28**	0.010	7.1
			10	**0.56**	0.005	1.7
			5	**0.38**	0.002	1.2
$N(CH_2COOH)_2$ containing polymer/Fe_3O_4 composite [12]	36.5	0.40	50	1.10	0.122	22.29
			20	**0.50**	0.049	19.6
			10	**0.20**	0.025	24.6
			5	**0.10**	0.012	24.6
Magnetic-powdered activated carbon [14]	n.d.	1.0	100	26		n.d.
Thiol-silica-coated magnetite [15]	207.7	0.008	80	**0.00**	n.a.	n.a.
Acrylamide-hydroxyl- MOFs [10]	333	0.05	100	20.0	1.6	16.05
			20	3.05	0.339	22.3
			10	1.65	0.167	20.3
			5	1.45	0.071	9.8
			2	**0.68**	0.026	7.8
			1	**0.57**	0.009	3.0
MOF-74-Zn [16]	63	0.1	50	23.9	0.261	2.19
			40	20.0	0.20	2.01
			20	13.8	0.062	0.90
			10	8.1	0.019	0.47
			5	4.5	0.005	0.22

4. Conclusions

Efficient Hg(II) sorbents based on magnetite particles have been prepared using a simple synthetic procedure from low-cost materials; cost per kilogram [64] was urea (USD $0.2), L-cysteine (USD $10), D-Glucose (USD $0.4), ethylene glycol (USD $0.5), and hydrated ferric chloride (USD $0.65). Utilizing cysteine as a functionalization reagent for magnetic sorbents is much more economic and simpler, compared with productions of functionalized magnetic sorbents via multistep material synthesis [12,13,15], expensive functionalization reagent, or high-purity chemicals [10,12,13,15,16]. These sorbents are easy to separate from aqueous media and demonstrate excellent recyclability metrics. Comparative studies were undertaken for uncoated Fe_3O_4, carbon-coated Fe_3O_4 ($C@Fe_3O_4$), and cysteine-functionalized carbon-coated Fe_3O_4 (Cys-$C@Fe_3O_4$) sorbent particles. The 500Cys-$C@Fe_3O_4$ sorbent, having optimum L-cysteine loadings, are highly selective for Hg(II) adsorption, are capable of removing 90% of Hg(II) within 10 min, and are effective even at ultralow metal concentrations. The carbon shell enhances the Hg(II) sorption capacity, preserves the integrity of the Fe_3O_4 core, and acts as a scaffold, allowing appendage of metal chelating L-cysteine to the particle surface. Surface modification of $C@Fe_3O_4$ by cysteine boosts the performance and selectivity of the materials, resulting in enhanced levels of Hg(II) removal with fast adsorption rates, at ultralow Hg(II) concentrations. Moreover, factors potentially influencing adsorption efficiency, such as pH and temperature, were comprehensively studied in respect to both kinetics and thermodynamics. The facile preparation, fast and impressive adsorption performance, good selectivity, ease of separation, and recyclability alludes to the high potential of Cys-$C@Fe_3O_4$ as a candidate for selective removal of Hg(II) contaminants from water sources and for its possible adoption in mainstream water treatment processes.

Supplementary Materials: The following are available online at http://www.mdpi.com/2076-3417/10/22/8262/s1, Table S1 %Breakthrough (BT, of %removal efficiency) and BT time interpolated from the %BT vs. treatment times plot in Figure 4, Table S2: %Breakthrough (BT, of %removal efficiency) and BT time interpolated from the %BT vs. treatment times plotted in Figure S2., Scheme S1: Synthesis process for uncoated Fe_3O_4, $C@Fe_3O_4$, and Cys-$C@Fe_3O_4$ samples. Figure S1: Nitrogen adsorption–desorption isotherms and pore size distribution plots (inset) for (a) uncoated Fe_3O_4, (b) C@ Fe_3O_4, (c) 250Cys-$C@Fe_3O_4$, (d) 500Cys-$C@Fe_3O_4$, and (e)1000Cys-$C@Fe_3O_4$. Figure S2: Hg(II) treatment time dependence of % Breakthrough (BT) at initial Hg(II) concentration of 1000 ppb and sorbent loading of 0.01 g L^{-1} at different pH values. High reproducibility of the measurements can be indicated by small standard deviations from five identical batch experiments. Figure S3: Linear fitting of (a) Langmuir and (b) Freundlich isotherms for Hg(II) adsorption onto uncoated Fe_3O_4, C@ Fe_3O_4, and 500Cys-C@ Fe_3O_4 and thermodynamic data for Hg(II) adsorption on 500Cys-C@ Fe_3O_4. Figure S4: Thermodynamic data for Hg(II) adsorption on 500Cys-C@ Fe_3O_4.

Author Contributions: Formal analysis, investigation, and writing—original draft preparation, A.S. Formal analysis, investigation, and writing—original draft preparation, T.B. Formal analysis, investigation, W.P.-O. Conceptualization, methodology, and supervision, T.S., K.U., and K.S. Writing—review and editing, S.C. Project administration, conceptualization, methodology, funding acquisition, and writing—review and editing, S.M.S. All authors have read and agreed to the published version of the manuscript.

Funding: This research was partially funded by the Thailand Science Research and Innovation (grant no. IRN62W0005). A.S. received the scholarship from the Royal Golden Jubilee Ph.D. Program (grant no. PHD/0119/2553).

Acknowledgments: The authors acknowledge financial support from the Thailand Science Research and Innovation through the Royal Golden Jubilee Ph.D. Program (grant no. PHD/0119/2553) and research grants (IRN62W0005). Instruments were provided by PTT Public Company Limited, Center of Excellence for Innovation in Chemistry (PERCH-CIC), and the Faculty of Science, Mahidol University.

Conflicts of Interest: The authors declare no conflicts of interest.

References

1. Jiang, G.-B.; Shi, J.B.; Feng, X.-B. Mercury pollution in China. An overview of the past and current sources of the toxic metal. *Environ. Sci. Technol.* **2006**, *40*, 3672–3678. [CrossRef]
2. Weisener, C.G.; Sale, K.S.; Smyth, D.J.A.; Blowes, D.W. Field column study using zerovalent iron for mercury removal from contaminated groundwater. *Environ. Sci. Technol.* **2005**, *39*, 6306–6312. [CrossRef]

3. Herrero, R.; Lodeiro, P.; Rey-Castro, C.; Vilariño, T.; Sastre de Vicente, M.E. Removal of inorganic mercury from aqueous solutions by biomass of the marine macroalga *Cystoseira baccata*. *Water Res.* **2005**, *39*, 3199–3210. [CrossRef] [PubMed]
4. Vikrant, K.; Kim, K.H. Nanomaterials for the adsorptive treatment of Hg(II) ions from water. *Chem. Eng. J.* **2019**, *358*, 264–282. [CrossRef]
5. Azimi, A.; Azari, A.; Rezakazemi, M.; Ansarpour, M. Removal of Heavy Metals from Industrial Wastewaters: A Review. *ChemBioEng Rev.* **2017**, *4*, 37–59. [CrossRef]
6. Bernhoft, R.A. Mercury toxicity and treatment: A review of the literature. *J. Environ. Public Health* **2012**, 460508. [CrossRef] [PubMed]
7. United Nations Environment Program. *Practical Sourcebook on Mercury Waste Storage and Disposal*; United Nations Environmental Program: Nairobi, Kenya, 2015.
8. The World Health Organization (WHO). *Guidelines for Drinking-Water Quality*, 3rd ed.; Directive 2000/60/EC of the European Parliament and of the Council; WHO: Geneva, Switzerland, 2000.
9. De Clercq, J. Removal of mercury from aqueous solutions by adsorption on a new ultra stable mesoporous adsorbent and on a commercial ion exchange resin. *Int. J. Ind. Chem.* **2012**, *3*, 13. [CrossRef]
10. Luo, F.; Chen, J.L.; Dang, L.L.; Zhou, W.N.; Lin, H.L.; Li, J.Q.; Liu, S.J.; Luo, M.B. High-performance Hg^{2+} removal from ultra-low-concentration aqueous solution using both acylamide- and hydroxyl-functionalized metal-organic framework. *J. Mater. Chem. A* **2015**, *3*, 9616–9620. [CrossRef]
11. Qu, Z.; Yan, L.; Li, L.; Xu, J.; Liu, M.; Li, Z.; Yan, N. Ultraeffective ZnS nanocrystals sorbent for mercury(II) Removal Based on Size-Dependent Cation Exchange. *ACS Appl. Mater. Interfaces* **2014**, *6*, 18026–18032. [CrossRef]
12. Qi, X.; Li, N.; Xu, Q.; Chen, D.; Li, H.; Lu, J. Water-soluble Fe_3O_4 superparamagnetic nanocomposites for the removal of low concentration mercury(II) ions from water. *RSC Adv.* **2014**, *4*, 47643–47648. [CrossRef]
13. Parham, H.; Zargar, B.; Shiralipour, R. Fast and efficient removal of mercury from water samples using magnetic iron oxide nanoparticles modified with 2-mercaptobenzothiazole. *J. Hazard. Mater.* **2012**, *205*, 94–100. [CrossRef] [PubMed]
14. Faulconer, E.K.; von Reitzenstein, N.V.H.; Mazyck, D.W. Optimization of magnetic powdered activated carbon for aqueous Hg(II) removal and magnetic recovery. *J. Hazard. Mater.* **2012**, *199–200*, 9–14. [CrossRef] [PubMed]
15. Hakami, O.; Zhang, Y.; Banks, C.J. Thiol-functionalised mesoporous silica-coated magnetite nanoparticles for high efficiency removal and recovery of Hg from water. *Water Res.* **2012**, *46*, 3913–3922. [CrossRef] [PubMed]
16. Xiong, Y.Y.; Li, J.Q.; Gong, L.L.; Feng, X.F.; Meng, L.N.; Zhang, L.; Meng, P.P.; Luo, M.B.; Luo, F. Using MOF-74 for Hg^{2+} removal from ultra-low concentration aqueous solution. *J. Solid State Chem.* **2017**, *246*, 16–22. [CrossRef]
17. Luo, H.; Zhang, S.; Li, X.; Liu, X.; Xu, Q.; Liu, J.; Wang, Z. Tannic acid modified Fe_3O_4 core–shell nanoparticles for adsorption of Pb^{2+} and Hg^{2+}. *J. Taiwan Inst. Chem. Eng.* **2017**, *72*, 163–170. [CrossRef]
18. Azari, A.; Gharibi, H.; Kakavandi, B.; Ghanizadeh, G.; Javid, A.; Hossein Mahvi, A.; Sharafia, K.; Khosravia, T. Magnetic adsorption separation process: An alternative method of mercury extracting from aqueous solution using modified chitosan coated Fe_3O_4 nanocomposites. *J. Chem. Technol. Biotechnol.* **2017**, *92*, 188–200. [CrossRef]
19. Kazemi, A.; Bahramifar, N.; Heydari, A.; Olsen, S.I. Synthesis and sustainable assessment of thiol-functionalization of magnetic graphene oxide and superparamagnetic $Fe_3O_4@SiO_2$ for Hg(II) removal from aqueous solution and petrochemical wastewater. *J. Taiwan Inst. Chem. Eng.* **2019**, *95*, 78–93. [CrossRef]
20. Zhang, Z.; Niu, Y.; Chen, H.; Yang, Z.; Bai, L.; Xue, Z.; Yang, H. Feasible one-pot sequential synthesis of aminopyridine functionalized magnetic Fe_3O_4 hybrids for robust capture of aqueous Hg(II) and Ag(I). *ACS Sustain. Chem. Eng.* **2019**, *7*, 7324–7337. [CrossRef]
21. Zhou, Y.; Luan, L.; Tang, B.; Niu, Y.; Qu, R.; Liu, Y.; Xu, W. Fabrication of Schiff base decorated PAMAM dendrimer/magnetic Fe_3O_4 for selective removal of aqueous Hg(II). *Chem. Eng. J.* **2020**, *398*, 125651. [CrossRef]
22. Fayazi, M. Removal of mercury(II) from wastewater using a new and effective composite: Sulfur-coated magnetic carbon nanotubes. *Environ. Sci. Pollut. Res.* **2020**, *27*, 12270–12279. [CrossRef]
23. Jeon, C.; Solis, K.L.; An, H.-R.; Hong, Y.; Igalavithana, A.D.; Ok, Y.S. Sustainable removal of Hg(II) by sulfur-modified pine-needle biochar. *J. Hazard. Mater.* **2020**, *388*, 122048. [CrossRef] [PubMed]
24. Xu, X.; Schierz, A.; Xu, N.; Cao, X. Comparison of the characteristics and mechanisms of Hg(II) sorption by biochars and activated carbon. *J. Colloid Interface Sci.* **2016**, *463*, 55–60. [CrossRef]
25. Wang, Y.; Mu, Y.; Zhao, Q.-B.; Yu, H.-Q. Isotherms, kinetics and thermodynamics of dye biosorption by anaerobic sludge. *Sep. Purif. Technol.* **2006**, *50*, 1–7. [CrossRef]

26. Tang, X.; Niu, D.; Bi, C.; Shen, B. Hg^{2+} Adsorption from a low-concentration aqueous solution on chitosan beads modified by combining polyamination with Hg2+-imprinted technologies. *Ind. Eng. Chem. Res.* **2013**, *52*, 13120–13127. [CrossRef]
27. Tang, S.C.N.; Lo, I.M.C. Magnetic nanoparticles: Essential factors for sustainable environmental applications. *Water Res.* **2013**, *47*, 2613–2632. [CrossRef] [PubMed]
28. Cheng, K.; Zhou, Y.-M.; Sun, Z.-Y.; Hu, H.-B.; Zhong, H.; Kong, X.-K.; Chen, Q.-W. Synthesis of carbon-coated, porous and water-dispersive Fe_3O_4 nanocapsules and their excellent performance for heavy metal removal applications. *Dalton Trans.* **2012**, *41*, 5854–5861. [CrossRef]
29. Xuan, S.; Hao, L.; Jiang, W.; Gong, X.; Hu, Y.; Chen, Z. A facile method to fabricate carbon-encapsulated Fe_3O_4 core/shell composites. *Nanotechnology* **2007**, *18*, 035602. [CrossRef]
30. Peniche, H.; Osorio, A.; Acosta, N.; de la Campa, A.; Peniche, C. Preparation and characterization of superparamagnetic chitosan microspheres: Application as a support for the immobilization of tyrosinase. *J. Appl. Polym. Sci.* **2005**, *98*, 651–657. [CrossRef]
31. Pan, B.-F.; Gao, F.; Gu, H.-C. Dendrimer modified magnetite nanoparticles for protein immobilization. *J. Colloid Interface Sci.* **2005**, *284*, 1–6. [CrossRef]
32. Zhao, W.; Gu, J.; Zhang, L.; Chen, H.; Shi, J. Fabrication of uniform magnetic nanocomposite spheres with a magnetic core/mesoporous silica shell structure. *J. Am. Chem. Soc.* **2005**, *127*, 8916–8917. [CrossRef]
33. Shen, X.; Wang, Q.; Chen, W.; Pang, Y. One-step synthesis of water-dispersible cysteine functionalized magnetic Fe3O4 nanoparticles for mercury(II) removal from aqueous solutions. *Appl. Surface Sci.* **2014**, *317*, 1028–1034. [CrossRef]
34. Zheng, J.; Liu, Z.Q.; Zhao, X.S.; Liu, M.; Liu, X.; Chu, W. One-step solvothermal synthesis of Fe3O4@C core–shell nanoparticles with tunable sizes. *Nanotechnology* **2012**, *23*, 165601. [CrossRef] [PubMed]
35. Wang, H.; Yu, Y.-F.; Chen, Q.-W.; Cheng, K. Carboxyl-functionalized nanoparticles with magnetic core and mesopore carbon shell as adsorbents for the removal of heavy metal ions from aqueous solution. *Dalton Trans.* **2011**, *40*, 559–563. [CrossRef] [PubMed]
36. Liu, Q.; Li, W.; Zhao, W.; Tan, L.; Jing, X.; Liu, J.; Song, D.; Zhang, H.; Li, R.; Liu, L.; et al. Synthesis of ketoxime-functionalized Fe3O4@C core-shell magnetic microspheres for enhanced uranium(VI) removal. *RSC Adv.* **2016**, *6*, 22179–22186. [CrossRef]
37. Azam, A.S.; Mohammad, A.A. Magnetic Fe_3O_4@C nanoparticles modified with 1-(2-thiazolylazo)-2-naphthol as a novel solid-phase extraction sorbent for preconcentration of copper (II). *Mikrochim. Acta* **2014**, *182*, 257–264. [CrossRef]
38. Xu, J.; Sun, Y.; Zhang, J. Solvothermal synthesis of Fe_3O_4 nanospheres for high-performance electrochemical non-enzymatic glucose sensor. *Sci. Rep.* **2020**, *10*, 16026. [CrossRef] [PubMed]
39. Zhu, M.; Diao, G. Synthesis of porous Fe_3O_4 nanospheres and its application for the catalytic degradation of xylenol orange. *J. Phys. Chem. C* **2011**, *115*, 18923–18934. [CrossRef]
40. Chang, R.; Goldsby, K.A. *Chemistry*, 11th ed.; McGraw-Hill Education: New York, NY, USA, 2012.
41. Eastman, E.D.; Rollefson, G.K. *Physical Chemistry*, 1st ed.; McGraw-Hill: New York, NY, USA, 1974; p. 307.
42. Borecki, M.; Korwin-Pawlowski, M.L.; Beblowska, M.; Szmidt, J.; Jakubowski, A. Optoelectronic Capillary Sensors in Microfluidic and Point-of-Care Instrumentation. *Sensors* **2010**, *10*, 3771–3797. [CrossRef]
43. Wei, X.; Liu, T.; Li, J.; Chen, X. A magnetic-controlled amperometric biosensor based on composite bio-particulates Fe_3O_4 and nano-au with the signal enhancement by increasing loading of horseradish peroxidase. *Int. J. Electrochem. Sci.* **2001**, *6*, 4953–4966.
44. Li, J.; Gao, H. A renewable potentiometric immunosensor based on Fe_3O_4 nanoparticles immobilized Anti-IgG. *Electroanalysis* **2008**, *20*, 881–887. [CrossRef]
45. Na, C.J.; Yoo, M.J.; Tsang, D.C.W.; Kim, H.W.; Kim, K.H. High-performance materials for effective sorptive removal of formaldehyde in air. *J. Hazard. Mater.* **2019**, *366*, 452–465. [CrossRef] [PubMed]
46. Shahzad, A.; Jang, J.; Lim, S.R.; Lee, D.S. Unique selectivity and rapid uptake of molybdenum-disulfide-functionalized MXene nanocomposite for mercury adsorption. *Environ. Res.* **2020**, *182*, 109005. [CrossRef] [PubMed]
47. Pham, X.N.; Nguyen, T.P.; Pham, T.N.; Tran, T.T.N.; Tran, T.V.T. Synthesis and characterization of chitosan coated magnetite nanoparticles and their application in curcumin drug delivery. *Adv. Nat. Sci. Nanosci. Nanotechnol.* **2016**, *7*, 045010. [CrossRef]

48. Li, C.; Wei, Y.; Liivat, A.; Zhu, Y.; Zhu, J. Microwave-solvothermal synthesis of Fe_3O_4 magnetic nanoparticles. *Mater. Lett.* **2013**, *107*, 23–26. [CrossRef]
49. Ren, W.; Ai, Z.; Jia, F.; Zhang, L.; Fan, X.; Zou, Z. Low temperature preparation and visible light photocatalytic activity of mesoporous carbon-doped crystalline TiO_2. *Appl. Catal. B Environ.* **2007**, *69*, 138–144. [CrossRef]
50. Fan, H.-L.; Li, L.; Zhou, S.-F.; Liu, Y.-Z. Continuous preparation of Fe3O4 nanoparticles combined with surface modification by L-cysteine and their application in heavy metal adsorption. *Ceram. Int.* **2016**, *42*, 4228–4237. [CrossRef]
51. Chen, T.; Zhang, X.; Qian, J.; Li, S.; Jia, X.; Song, H.J. One-step hydrothermal synthesis of carbon@Fe_3O_4 nanoparticles with high adsorption capacity. *J. Mater. Sci. Mater. Electron.* **2014**, *25*, 1381–1387. [CrossRef]
52. Tran, L.; Wu, P.; Zhu, Y.; Liu, S.; Zhu, N. Comparative study of Hg(II) adsorption by thiol- and hydroxyl-containing bifunctional montmorillonite and vermiculite. *Appl. Surf. Sci.* **2015**, *356*, 91–101. [CrossRef]
53. Tran, L.; Wu, P.; Zhu, Y.; Yang, L.; Zhu, N. Highly enhanced adsorption for the removal of Hg(II) from aqueous solution by Mercaptoethylamine/Mercaptopropyltrimethoxysilane functionalized vermiculites. *J. Colloid Interface Sci.* **2015**, *445*, 348–356. [CrossRef]
54. Li, B.; Zhang, Y.; Ma, D.; Shi, Z.; Ma, S. Mercury nano-trap for effective and efficient removal of mercury(II) from aqueous solution. *Nat. Commun.* **2014**, *5*, 5537. [CrossRef]
55. Husnain, S.M.; Kim, J.-H.; Lee, C.S.; Chang, Y.-Y.; Um, W.; Chang, Y.-S. Superparamagnetic nalidixic acid grafted magnetite (Fe_3O_4/NA) for rapid and efficient mercury removal from water. *RSC Adv.* **2016**, *6*, 35825–35832. [CrossRef]
56. Rinzin, U.; Singjai, P.; Wilairat, P.; Meejoo, S. Mechanochemical treated multi-walled carbon nanotubes for incorporation of metal ions. *Adv. Mater. Res.* **2008**, *55*, 537–540. [CrossRef]
57. Pan, S.; Shen, H.; Xu, Q.; Luo, J.; Hu, M. Surface mercapto engineered magnetic Fe_3O_4 nanoadsorbent for the removal of mercury from aqueous solutions. *J. Colloid Interface Sci.* **2012**, *365*, 204–212. [CrossRef] [PubMed]
58. Kamari, A.; Yusoff, S.N.M.; Abdullah, F.; Putra, W.P. Biosorptive removal of Cu(II), Ni(II) and Pb(II) ions from aqueous solutions using coconut dregs residue: Adsorption and characterisation studies. *J. Environ. Chem. Eng.* **2014**, *2*, 1912–1919. [CrossRef]
59. Tsai, W.-C.; de Luna, M.D.G.; Bermillo-Arriesgado, H.L.P.; Futalan, C.M.; Colades, J.I.; Wan, M.-W. Competitive fixed-bed adsorption of Pb(II), Cu(II), and Ni(II) from aqueous solution using chitosan-coated bentonite. *Int. J. Polym. Sci.* **2016**, *2016*, 1608939. [CrossRef]
60. Li, Q.; Wang, Z.; Fang, D.-M.; Qu, H.-Y.; Zhu, Y.; Zou, H.-J.; Chen, Y.-R.; Du, Y.-P.; Hu, H.-L. Preparation, characterization, and highly effective mercury adsorption of L-cysteine-functionalized mesoporous silica. *New J. Chem.* **2014**, *38*, 248–254. [CrossRef]
61. Jeon, C.; Ha Park, K. Adsorption and desorption characteristics of mercury(II) ions using aminated chitosan bead. *Water Res.* **2005**, *39*, 3938–3944. [CrossRef]
62. Kyzas, G.; Deliyanni, E. Mercury(II) Removal with modified magnetic chitosan adsorbents. *Molecules* **2013**, *18*, 6193–6214. [CrossRef]
63. Javadian, H.; Taghavi, M. Application of novel Polypyrrole/thiol-functionalized zeolite Beta/MCM-41 type mesoporous silica nanocomposite for adsorption of Hg^{2+} from aqueous solution and industrial wastewater: Kinetic, isotherm and thermodynamic studies. *Appl. Surf. Sci.* **2014**, *289*, 487–494. [CrossRef]
64. Alibaba Supplier. Available online: https://offer.alibaba.com (accessed on 18 November 2020).